Journal of
Marine Science and Engineering

MDPI

Article

Numerical Investigation on the Dynamics of Mixture Transport in Flexible Risers during Deep-Sea Mining

Lei Liu [1,2], Kangyu Gai [2], Jianmin Yang [1,2] and Xiaoxian Guo [1,2,*]

1 State Key Laboratory of Ocean Engineering, Shanghai Jiao Tong University, Shanghai 200240, China
2 Sanya Yazhou Bay Institution of Deep-Sea Sci-Tech, Shanghai Jiao Tong University, Sanya 572000, China
* Correspondence: xiaoxguo@sjtu.edu.cn; Tel.: +86-021-3420-7050

Abstract: Mixture transport from a seabed mining vehicle to a buffer is a key procedure in deep-sea mining. Dynamic performances of the particle–seawater mixture in a single-peak flexible riser were numerically investigated using computational fluid dynamics and the discrete element method. Both the time-averaged local characteristics and the instantaneous flow behaviors in the riser are presented. The effects of key parameters, such as feeding concentration and mixture transport velocity, were evaluated by a sensitivity analysis. Large local concentration accompanied by small particle velocity occurs in the ascending sections and increases the risk of blockage. The particle–wall contact reaches the maximum value at both the peak and trough of the single-peak riser. A small feeding concentration would reduce both particle–wall contact, and hydraulic gradient, whereas a moderate mixture transport velocity may be appropriate for the transport in terms of operation safety and energy efficiency. In addition, the mixture transport in a double-peak riser was simulated to examine which configuration is better for engineering applications. The lower maximum local concentration, particle–wall contact and hydraulic gradient and the larger minimum particle velocity indicate that a double-peak flexible riser may be more suitable for the mixture transport.

Keywords: deep-sea mining; mixture transport; flexible riser; numerical simulation

check for updates

Citation: Liu, L.; Gai, K.; Yang, J.; Guo, X. Numerical Investigation on the Dynamics of Mixture Transport in Flexible Risers during Deep-Sea Mining. *J. Mar. Sci. Eng.* **2022**, *10*, 1842. https://doi.org/10.3390/jmse10121842

Academic Editor: Anabela Oliveira

Received: 1 November 2022
Accepted: 22 November 2022
Published: 1 December 2022

1. Introduction

The seabed deposits were first discovered in the 19th century by the H.M.S. Challenger [1]. According to the vast reservation and high grade, deep-sea mineral resources are regarded as alternatives to terrestrial mining with the increasing consumption of natural resources worldwide [2]. Three kinds of commercially valuable seabed mineral resources, including massive sulfide deposits, cobalt-rich ferromanganese crusts, and manganese nodules have been distinguished at depths up to several kilometers, and the distributions have been summarized by Hannington et al. [3]. As an example, manganese nodules are distributed on the flat seafloor within the first 10 cm of the seabed sediments [4]. The abundant manganese, nickel, and cobalt make the mineral resources have commercial potential for industrial applications [5]. In the 1960s, the concept of deep-sea mining has been proposed to meet the requirements of natural resources for industrial production [6]. Since then, researchers and engineers have been focusing on the design and optimization of deep-sea mining systems, and fruitful achievements have been made in the past decades [7–11]. As shown in Figure 1, a typical deep-sea mining system consists of a mining vehicle on the seabed, a supporting vessel on the sea surface, and an ore transporting system composed of a vertical rigid pipe, a pump, a buffer, and a flexible riser [4,12]. The seabed deposits are collected and crushed by a mining vehicle, and then are transported to a freely hanging buffer via the flexible riser. A several-kilometer vertical rigid pipe is used to connect the buffer and the supporting vessel and to pump the particles to the sea surface. Among the overall configuration, the flexible riser is an essential part to cater the seabed topography and the movement of the mining vehicle. Owing to the large curvature at the peak and trough of the flexible riser, the mixture transport should be emphatically considered to avoid the blockage.

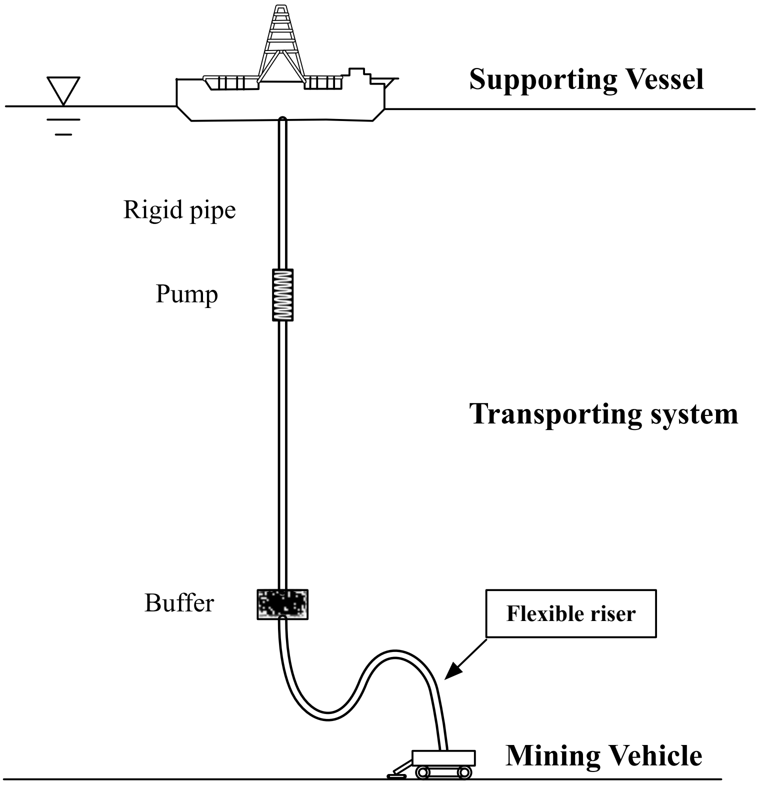

Figure 1. Sketch of a typical deep-sea mining system.

Research on the mixture flow in a flexible riser based on the background of deep-sea mining started in the late 20th century [13–21]. Abundant experimental facilities [13–15], numerical methods [16,17], and empirical formulas [18,19] have been developed to calculate pressure loss or hydraulic gradient during mixture transport and to examine the influences of various factors. In general, the key factors can be divided into three series, including the particle properties (e.g., particle diameter and density), the riser properties (e.g., spatial configuration and inner diameter), and the transport parameters (e.g., feeding concentration and mixture transport velocity). Feeding concentration clearly defines the level of pressure loss of deep-sea mining system [13]. The influence of the feeding concentration is remarkably consistent across the published works from both experiments and numerical simulations. A larger feeding concentration would result in a larger hydraulic gradient (or pressure loss, head loss) [14–16] irrespective of the riser configuration. It was found that as long as the feeding concentration is above 8%, the specific energy consumption is relatively insensitive to the feeding concentration [17]. Considering specific risers, a range of 10∼25% was suggested from the numerical simulations [16], whereas an optimal range of 10∼15% was proposed via empirical formulas from the viewpoints of efficiency and safety of the mixture transport [18]. According to numerical and experimental results, a suitable range of V_m should be identified based on the specific flexible risers. A superficial velocity increases the fluid–wall interaction, whereas a low transport velocity may cause the blockage in the riser [14,19]. At a high flow rate, the particles move at the center of the riser, leading to a hydraulic gradient close to that of water [19]. A mixture transport velocity of 5 times the largest particle settling velocity is suggested from numerical simulations [17]. Based on the specific risers, a range of 2.5∼4 m/s was proposed via numerical simulations [16], and a close range of critical flow velocity of 2.8∼3.6 m/s was recommended from empirical formulas [18].

As for the influences of particle properties, a small particle diameter would reduce the critical flow velocity and lower the pressure drop for the successful mixture transport [14,18]. However, in different configurations of the riser, different or even opposite conclusions were drawn from the experimental results [15]. Additionally, the particle size distribution and particle density would contribute to the pressure drop [13], and the system needs to be designed and optimized by considering the maximum density of the mixture.

The spatial configuration adjusted by the distribution of buoyancy layout has significant impacts on pressure loss [16]. As summarized from experimental results, the pressure drop of the mixture would be 1.5∼1.8 times that of the clear water at typical bend angles and bend radius [20]. In order to avoid blockage and reduce energy consumption, the critical flow velocity should be controlled according to the different relative distances between the buffer and mining vehicle [18].

The early investigations on the hydraulic transport of coarse particles were mainly conducted by experimental and theoretical methods. Due to the rapid development of numerical methods and computing power, numerical simulations on solid–liquid two-phase flow have been widely carried out with high credibility and accuracy. A review of the methods for estimating the pressure drop and the solid–liquid two-phase flow regimes in the flexible riser was performed by Parenteau [21]. The computational fluid dynamics (CFD) method was then conducted to understand transient behavior and predict pressure and power for the wave-shaped riser. Further, the coupling of CFD and discrete element method (DEM) was proposed to improve the accuracy of numerical results. Based on the background of deep-sea mining, CFD-DEM has been widely applied to simulate the mixture transport, e.g., in the vertical and horizontal rigid pipes [22–25], the Y-shaped elbow [26], and the pumps [27]. Similarly, pipeline transport of slurry shield under gravel stratum was investigated in inclined pipes [28]. However, numerical simulations on the mixture transport in flexible risers have not been well documented.

The previous studies mainly focused on the overall hydraulic gradient or pressure loss during mixture transport. From the aspect of safety in offshore operations, the local characteristics of the mixture are of great importance, because an excessive local concentration and a small particle velocity would result in the occasional blockage in the riser. This will interrupt the only channel for mixture transport and bring the entire deep-sea mining systems to a complete stop. However, to the best of our knowledge, the investigations on the dynamics of mixture transport in a flexible riser are not fruitful in the previous studies. Therefore, we conduct a comprehensive study on the local characteristics of the mixture in a flexible riser from both time-averaged and instantaneous perspectives using the CFD-DEM method. Overall descriptions of the particle velocity, local concentration, particle–wall contact, and the waterhead along the longitudinal direction of the riser are illustrated, followed by the instantaneous contours of particle and flow characteristics in both cross and longitudinal sections at typical locations. Sensitivity analyses are carried out for key parameters, such as mixture transport velocity and feeding concentration. In addition, dynamics of mixture transport in the single-peak riser and the double-peak riser are compared to provide references for the selection of riser configuration during deep-sea mining in terms of the inner mixture flow.

The remainder of this paper is organized as follows. The mathematical formulas for the numerical method are presented in Section 2. The overview of the numerical model and a convergence study for the spatial and temporal resolutions are provided in Section 3. The results and discussion are described in Section 4. Finally, the concluding remarks are summarized in Section 5.

2. Mathematical Formulas

2.1. Governing Equations

The incompressible fluid is governed by the Navier–Stokes (N-S) equations as follows.

$$\nabla \cdot \boldsymbol{u} = 0 \tag{1}$$

$$\frac{\partial \boldsymbol{u}}{\partial t} + \boldsymbol{u} \cdot \nabla \boldsymbol{u} = -\frac{1}{\rho_f} \nabla p + \nu \nabla^2 \boldsymbol{u} + \boldsymbol{g} + \boldsymbol{f_{sf}} \tag{2}$$

where $\boldsymbol{u}$ is the fluid velocity, p represents the pressure, ρ_f labels the density of the fluid, ν is the kinematic viscosity, t is the time and $\boldsymbol{g}$ denotes the gravitational acceleration. $\boldsymbol{f_{sf}}$ is particle-to-fluid force, which represents the momentum exchange between fluid and particle. In the present study, the Reynolds number of the inner flow would be in an approximate range of $5 \times 10^5 \sim 1.2 \times 10^6$, and fully-developed turbulence would occur in the flexible riser.

A six-degree-of-freedom (6DOF) motion solver is adopted to calculate particle motion in response to the fluid-to-particle forces, particle collisions, and gravity.

$$m_s \frac{d\boldsymbol{V_s}}{dt} = m_s \boldsymbol{g} + \boldsymbol{F_{fs}} + \boldsymbol{F_{ct}} \tag{3}$$

$$\boldsymbol{I_s} \frac{d\boldsymbol{\omega_s}}{dt} = \boldsymbol{M_{ct}} + \boldsymbol{M_{fs}} \tag{4}$$

where m_s represents the particle mass, $\boldsymbol{V_s}$ demotes the particle velocity, $\boldsymbol{I_s}$ is the moment of inertia of the particle, and $\boldsymbol{\omega_s}$ is the particle's angular velocity. $\boldsymbol{F_{fs}}$ and $\boldsymbol{M_{fs}}$ are the fluid-to-particle force and moment, respectively. $\boldsymbol{F_{ct}}$ and $\boldsymbol{M_{ct}}$ are the contact force and moment, respectively, caused by the particle–particle and particle–wall collisions.

2.2. Fluid-Particle Interaction

The fluid force $\boldsymbol{F_{fs}}$ exerted on the particle can be represented by Equation (5).

$$\boldsymbol{F_{fs}} = \boldsymbol{F_d} + \boldsymbol{F_l} + \boldsymbol{F_p} + \boldsymbol{F_{am}} + \boldsymbol{F_B} \tag{5}$$

where $\boldsymbol{F_d}$ is the drag force, $\boldsymbol{F_l}$ is the lift force, $\boldsymbol{F_p}$ is the pressure gradient force and $\boldsymbol{F_{am}}$ is the added mass force. The time-dependent Basset force $\boldsymbol{F_B}$ is not considered owing to its marginal effect on the particles in the present study.

The drag force $\boldsymbol{F_d}$ can be calculated as follows [29].

$$\boldsymbol{F_d} = \frac{1}{8} C_d \rho_f (\boldsymbol{u_f} - \boldsymbol{V_s})^2 \pi d^2 \tag{6}$$

$$C_d = \left(0.63 + \frac{4.80}{\sqrt{\varepsilon_i Re_p}}\right)^2 \varepsilon_i^{2-\xi} \tag{7}$$

$$\xi = 3.7 - 0.65\exp\left[-\frac{(1.5 - \log_{10}(\varepsilon_i Re_p))^2}{2}\right] \tag{8}$$

where $\boldsymbol{u_f}$ is the fluid velocity around the particle, d is the particle diameter, ε_i is the void fraction around a particle, C_d is the drag coefficient, Re_p is the particle Reynolds number. $\varepsilon_i^{-\xi}$ represents the effect of enhanced drag on a particle due to the presence of other particles around it.

The lift force $\boldsymbol{F_l}$ can be divided into the Magnus force $\boldsymbol{F_{LM}}$ and the Saffman force $\boldsymbol{F_{LS}}$ [30]. The former is caused by the rotation of the particle, whereas the latter results from the shear rate of the fluid.

$$\boldsymbol{F_{LM}} = C_{LM}\frac{\rho_f \pi}{8}d^2|\boldsymbol{u_f} - \boldsymbol{V_s}|\frac{(\boldsymbol{\omega_f} - \boldsymbol{\omega_s}) \times (\boldsymbol{u_f} - \boldsymbol{V_s})}{|\boldsymbol{\omega_f} - \boldsymbol{\omega_s}|} \tag{9}$$

$$C_{LM} = 0.45 + \left(\frac{Re_{rot}}{Re_p} - 0.45\right)e^{-0.5684 Re_{rot}^{0.4} Re_p^{0.3}} \tag{10}$$

where C_{LM} is the coefficient of Magnus lift force, $(\boldsymbol{\omega_f} - \boldsymbol{\omega_s})$ is the relative angular velocity of the particle to the fluid, Re_{rot} is the rotational Reynolds number.

$$\boldsymbol{F_{LS}} = C_{LS}\frac{\rho_f \pi}{8}d^3(\boldsymbol{u_f} - \boldsymbol{V_s}) \times 2\boldsymbol{\omega_f} \tag{11}$$

$$C_{LS} = \frac{4.1126}{\sqrt{Re_s}}\Phi(Re_p,\ Re_s) \tag{12}$$

where C_{LS} is the shear lift coefficient and Re_s is the shear Reynolds number. $\Phi(Re_p,\ Re_s)$ is the function about $(Re_p,\ Re_s)$ and can be calculated as follows.

$$\Phi(Re_p,\ Re_s) = \begin{cases} (1 - 0.3314\sqrt{\dfrac{Re_s}{2Re_p}})e^{-0.1Re_p} + 0.3314\sqrt{\dfrac{Re_s}{2Re_p}} & (Re_p \leqslant 40) \\ 0.0524\sqrt{0.5Re_s} & (Re_p > 40) \end{cases} \tag{13}$$

The pressure gradient force $\boldsymbol{F_p}$ can be represented by Equation (14).

$$\boldsymbol{F_p} = -\forall \nabla p_{static} \tag{14}$$

where $\forall$ is the particle volume and ∇p_{static} is the static pressure gradient.

The added mass force $\boldsymbol{F_{am}}$ is calculated as follows [31].

$$\boldsymbol{F_{am}} = C_{am}\rho_f \forall \frac{d}{dt}(\boldsymbol{u_f} - \boldsymbol{V_s}) \tag{15}$$

where $C_{am} = 0.5$ is the coefficient of added mass for a spherical particle.

2.3. Contact Model for Particle–Particle and Particle–Wall Collisions

$\boldsymbol{F_{ct}}$ and $\boldsymbol{M_{ct}}$ are the sum of contact force and moment, respectively, caused by other particles.

$$\boldsymbol{F_{ct}} = \sum \boldsymbol{F_c} \tag{16}$$

$$\boldsymbol{M_{ct}} = \sum(\boldsymbol{r_c} \times \boldsymbol{F_c} + \boldsymbol{M_c}) \tag{17}$$

where $\boldsymbol{F_c}$ and $\boldsymbol{M_c}$ represent the contact force and moment, respectively, between two individual particles, and $\boldsymbol{r_c}$ is the vector from the particle center to the contact point.

In the present study, the Hertz–Mindlin no-slip contact model is adopted to simulate particle contact. The forces at the contact point are calculated by the spring–dashpot model in both normal and tangential directions (see Equation (18)). The spring provides the stiffness and generates the repulsive force to push the contacting particles apart; the dashpot provides viscous damping and allows imperfect elastic collisions. The spring accounts for the elastic part of the response, whereas the dashpot accounts for the energy dissipation during the collision.

$$\boldsymbol{F_c} = \boldsymbol{F_n} + \boldsymbol{F_t} \tag{18}$$

where $\boldsymbol{F_n}$ is the normal and $\boldsymbol{F_t}$ is the tangential force component.

The normal force $\boldsymbol{F_n}$ is defined by the following:

$$F_n = -K_n d_n - N_n v_n \tag{19}$$

where d_n is the overlap in the normal direction, v_n is the normal velocity component of the relative particle surface velocity at the contact point. K_n and N_n are the spring stiffness and viscous damping, respectively, in the normal direction, and can be calculated as follows.

$$K_n = \frac{4}{3} E_{eq} \sqrt{d_n R_{eq}} \tag{20}$$

$$N_n = \sqrt{5 K_n M_{eq}} N_{n\ damp} \tag{21}$$

$$N_{n\ damp} = \frac{-ln(C_{n\ rest})}{\sqrt{\pi^2 + ln(C_{n\ rest})^2}} \tag{22}$$

where E_{eq}, R_{eq}, and M_{eq} are equivalent to Young's Modulus, radius, and particle mass, respectively; $N_{n\ damp}$ is the normal damping coefficient and $C_{n\ rest}$ is the normal coefficient of restitution.

The tangential force F_t is defined by the following:

$$F_t = \begin{cases} -K_t d_t - N_t v_t & |K_t d_t| < |K_n d_n| C_{fs} \\ \dfrac{|K_n d_n| C_{fs} d_t}{|d_t|} & |K_t d_t| \geqslant |K_n d_n| C_{fs} \end{cases} \tag{23}$$

where C_{fs} is the static friction coefficient, d_t is the overlap in the tangential direction, v_t is the tangential velocity component of the relative particle surface velocity at the contact point. K_t and N_t are the stiffness and damping, respectively, in the tangential direction.

$$K_t = 8 G_{eq} \sqrt{d_t R_{eq}} \tag{24}$$

$$N_t = \sqrt{5 K_t M_{eq}} N_{t\ damp} \tag{25}$$

$$N_{t\ damp} = \frac{-ln(C_{t\ rest})}{\sqrt{\pi^2 + ln(C_{t\ rest})^2}} \tag{26}$$

where G_{eq} is the equivalent shear modulus; $N_{t\ damp}$ is the tangential damping coefficient and $C_{t\ rest}$ is the tangential coefficient of restitution.

More detailed descriptions of the Hertz–Mindlin contact model can be found in the references [32–34].

3. Numerical Model

3.1. Overview of Numerical Model

Depending on the depth differences in the mining site, the configuration of the riser would be affected. In order to make the numerical simulation more valuable and practical, we select a typical single-peak flexible riser designed for a field test at the depth of approximately 1000 m. From the viewpoints of reducing both the axial tension in the riser and the loads on the mining vehicle, the configuration is calculated and then optimized with the parameters from the initial design of the deep-sea mining system, as shown in Figure 2. A span of 125 m and a vertical height of 50 m from the seabed are adopted in the numerical model. The total length of the riser is 220.24 m. According to the designed production rate of approximately 1.5×10^6 tons per year for the ores, the inner diameter of the riser D = 0.2912 m is selected considering the mixture transport velocity of $V_{m0} \approx 5$ m/s and the feeding concentration of $C_{v0} \approx 9\%$ in the stable operating conditions. Owing to the small moving velocity and the limited migration of both the inlet (connected to the mining vehicle) and the outlet (connected to the buffer) of the riser, the deformation of the configuration is finite and has little effect on the inner mixture. Therefore, the deformation of the flexible riser is neglected in the present study. The numerical simulation is conducted by the multiphysics CFD software Simcenter STAR-CCM+.

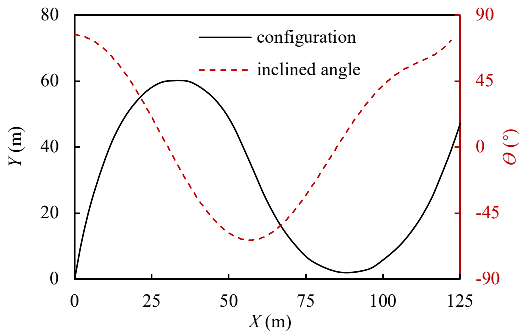

Figure 2. Spatial configuration of a single-peak flexible riser.

During the mixture transport, a set of monitors are designed with the diameter of $D = 0.2912$ m and the length of $L = 1$ m, as shown in Figure 3 and Table 1. Both the instantaneous and the time-averaged results of the local characteristics such as particle velocity V_{xl}, particle volume concentration C_{vl} and particle–wall contact force F_c are captured.

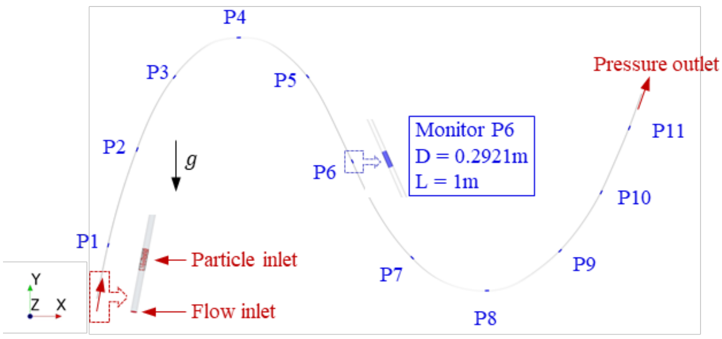

Figure 3. Computational domain and boundary conditions.

Table 1. Positions and inclined angles of the monitors in the single-peak riser.

Monitor	Position (x, y) (m)	Inclined Angle (°)	Monitor	Position (x, y) (m)	Inclined Angle (°)
P1	(2.39, 11.82)	75.48	P7	(71.99, 9.82)	−40.56
P2	(8.97, 33.92)	67.29	P8	(86.01, 2.08)	0
P3	(17.40, 50.66)	47.15	P9	(106.08, 10.73)	50.39
P4	(32.02, 60.11)	0	P10	(115.52, 24.03)	65.28
P5	(47.98, 51.59)	−56.67	P11	(122.05, 38.87)	69.94
P6	(58.40, 32.05)	−64.74			

Inclined angle: the angle between the flow direction in a monitor and the positive x–direction.

A velocity inlet boundary condition is adopted to model the fluid inlet at the start point of the riser. The particle injector is placed apart from the fluid inlet at a distance of 2 m to "minish" the numerical errors resulting from the interaction of two different inlet conditions on the same surface. The wall of the riser is set as a no-slip wall condition. A pressure outlet boundary condition is applied to the outlet of the mixture.

Figure 4 shows the grid structures of the computational domain. The riser is divided into approximately 2000 elements in the longitudinal direction; the boundary layer is modeled by prism layer cells and the inner flow domain is simulated by polyhedral cells.

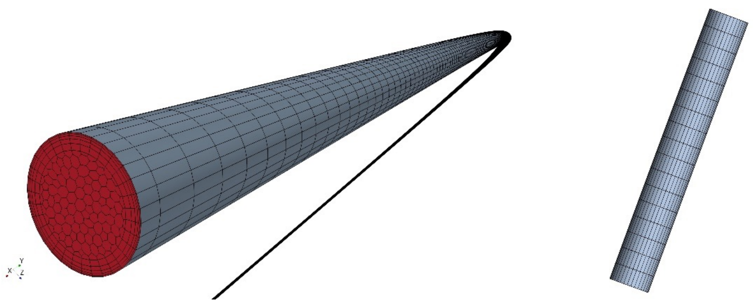

(**a**) Cross section. (**b**) Longitudinal section.

Figure 4. Grid structures of the computational domain.

Without loss of generality, the ambient fluid in the riser is set as the seawater with the density of $\rho_f = 1025\ \mathrm{kg/m^3}$ and the dynamic viscosity of $\mu_f = 0.001599$ Pa·s, which were measured in a specific site from a field test. The fluid is calculated by Reynolds Averaged Navier–Stokes (RANS) method with the turbulence modeled by the realizable k-ε model. The second-order temporal and spatial discretizations are adopted. During the simulation, the convective Courant number is no more than 0.5 in most discretized cells.

In the actual operation, the deposits on the seabed are first crushed to a smaller size before being injected into the riser. In the present study, the ores are simplified as spherical particles with a uniform diameter of $d = 20$ mm and a density of $\rho_s = 2000\ \mathrm{kg/m^3}$. The detailed parameters of the particle model are listed in Table 2, including particle properties, fluid force model, and coefficients for DEM. Noting that the coefficients, e.g., Young's modulus and the static friction coefficient are not accurately consistent with the real particles. However, the physical laws summarized from the calculated results are unified and sufficient for a rough estimation in the initial stage of engineering design.

Table 2. Particle property and parameters for the DEM model.

	Particle Model	**Value**
Particle property	Density	$2000\ \mathrm{kg/m^3}$
	Poisson's ratio	0.33
	Young's modulus	2.4×10^{10} Pa
Force model	Drag	See Equation (8)
	Shear lift	See Equation (12)
	Spin lift	See Equation (10)
	Added mass coefficient	0.5
DEM phase interaction	Contact model	Hertz–Mindlin, see Section 2.3
	Static friction coefficient, C_{fs}	0.3
	Normal restitution coefficient, $C_{n\ rest}$	0.5
	Tangential restitution coefficient, $C_{t\ rest}$	0.5

3.2. Convergence Study and Method Validation

In order to minimize the numerical errors caused by the grid structures and the time steps, the convergence study on the spatial and temporal resolutions was first conducted. The feeding concentration of $C_{v0} = 0.09$ and the mixture transport velocity of $V_{m0} = 5$ m/s were selected. Six meshes and seven time-steps were utilized for the numerical models. The most concerning characteristics, e.g., local concentration C_{vl} and particle velocity V_{xl} at the peak (Monitor P4) and in the middle of the descending section (Monitor P6) of the riser were selected for evaluation. As shown in Figure 5, with the increase of cell number from 5×10^5 to 2×10^6, both C_{vl} and V_{xl} change slightly. Meanwhile, the smaller time-step than 0.01s ($1/t > 100\ \mathrm{s^{-1}}$) would have a negligible effect on the results. Considering both the accuracy and the computing resources, the grid structure with a total cell number of approximate 500,000 and the time-step of 0.01 s are sufficient for the present simulations.

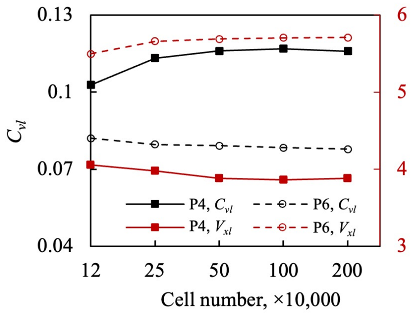

(**a**) Spatial resolution.

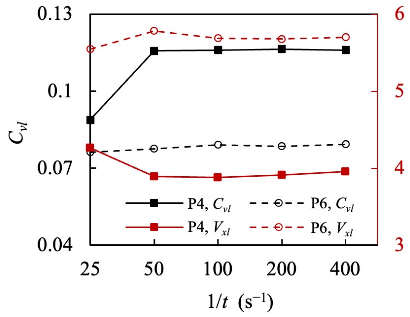

(**b**) Temporal resolution.

Figure 5. Convergence study of spatial and temporal resolutions.

Method validation was performed subsequently. No perfectly matched experimental data for the mixture transport in the flexible riser with the same configuration were found in the published works. Therefore, two simplified cases were simulated to validate both particle–fluid interaction and particle contact: a vertical hydraulic transport case for evaluating particle–fluid interaction and a horizontal particle-conveying case for assessing particle–particle and particle–wall interactions. The results were then compared to the experimental data from Xia et al. [11] and Ravelet et al. [25], respectively. Owing to the lack of measured C_{vl} in the experiments, the overall hydraulic gradient I was utilized to assess the accuracy of the numerical method.

In the horizontal pipe, the calculated hydraulic gradient agrees well with the experimental data in a wide range of mixture transport velocity (2∼5 m/s), as shown in Figure 6a. In the vertical case, the numerical results are slightly smaller than the experimental hydraulic gradient, which may result from the differences in the wall properties, e.g., the roughness and Young's modulus, between the simulations and the experiments. However, the general trends are the same and deviations are acceptable. According to the vertical and horizontal cases, it is drawn that both particle–fluid interaction and particle contact can be feasibly modeled, indicating the effectiveness of the CFD-DEM method for estimating the dynamics of the mixture in the riser.

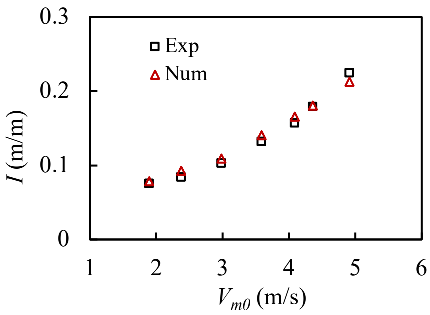

(**a**) Horizontal hydraulic transport.

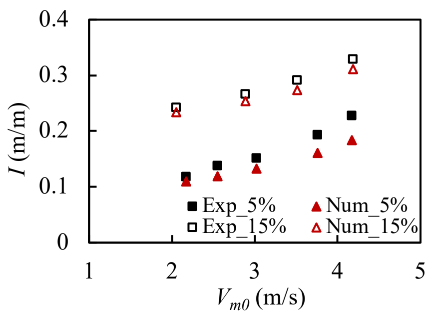

(**b**) Vertical hydraulic transport

Figure 6. Comparison between numerical results and published experimental data [11,25].

4. Results and Discussion

In this section, the characteristics of the mixture in the riser are discussed in terms of statistical analysis and instantaneous flow regimes. The influences of transport parameters, e.g., feeding concentration C_{v0} and mixture transport velocity V_{m0} are evaluated afterward. Finally, comparisons are made to a double-peak flexible riser to provide a preliminary reference to the selection of riser configuration in deep-sea mining.

4.1. Overall Description of the Mixture Transport

First, an overall description of the mixture transport in the single-peak flexible riser is analyzed with the input parameters of $C_{v0} = 0.09$ and $V_{m0} = 5$ m/s. For the sake of simplicity, the single-peak riser is divided into three sections: the first ascending section ($0 < x < 32$ m), the descending section ($32 < x < 89$ m) and the second ascending section ($32 < x < 125$ m). Figure 7 shows the time-averaged local characteristics of the mixture along the longitudinal direction of the riser in a stable transport state, including local concentration C_{vl}, particle velocity V_{xl}, particle–wall contact F_c, and local waterhead H.

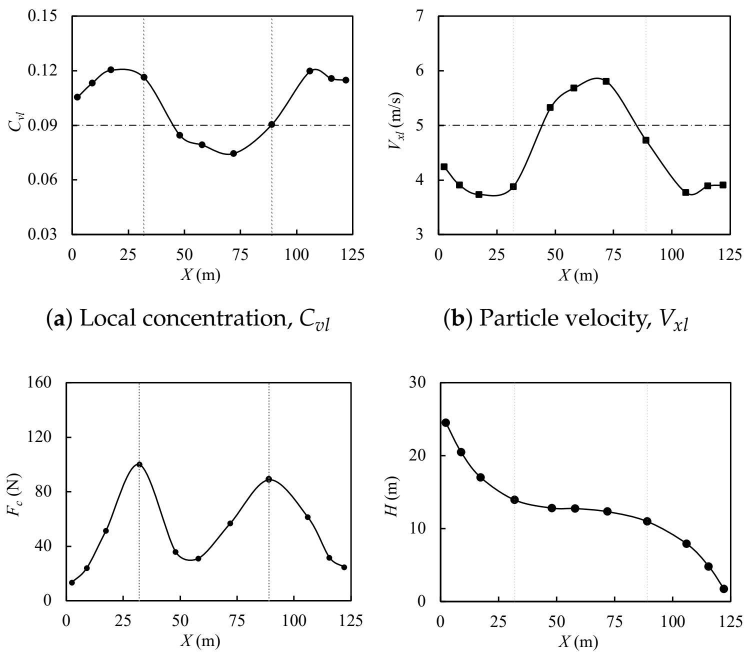

(**a**) Local concentration, C_{vl} (**b**) Particle velocity, V_{xl}

(**c**) Particle–wall contact force, F_c (**d**) Waterhead, H

Figure 7. Time-averaged local characteristics of the mixture in the riser at $C_{v0} = 0.09$, $V_{m0} = 5$ m/s. The vertical dashed lines represent the peak and trough of the riser.

In the ascending sections, the particles move upwards against gravity and particle–wall contact under the action of fluid forces. Owing to the larger density of the particle than the ambient fluid, a number of particles settle and accumulate on the lower side of the riser wall, and then are transported as bed load. Therefore, the local concentration C_{vl} is always larger than the feeding concentration C_{v0} (Figure 7a), whereas the particle velocity V_{xl} is smaller than the mixture transport velocity V_{m0} (Figure 7b). The maximum $C_{vl} = 0.12$ (approximate 1.34 C_{v0}) accompanied by the minimum $V_{xl} = 3.74$ m/s (approximate 0.75 V_{m0}) occurs just ahead of the peak. Meanwhile, an obvious reduction of waterhead H is observed in Figure 7c owing to the energy consumption of the mixture to compensate for the mixture–wall interaction and the gravitational potential energy of particles. At the peak of the riser, one can find a slight reduction of C_{vl} and a tiny increase of V_{xl} resulting from the rapid mitigation of particle accumulation in the coming descending section. However, the particle–wall contact force F_c reaches the maximum value of 100.2 N ($\approx$1.74 F_b, see Figure 7d. F_b represents the reduced gravity of the transported particles in the monitors and can be expressed by $F_b = C_{v0}(\rho_s - \rho_f)g\pi LD^2/4$), because most of the particles would be hindered by the large curvature and travel as bed load on the riser wall.

In the descending section, gravity becomes the driving force on the mixture and the particles are accelerated and dispersed rapidly. As shown in Figure 7, the particle velocity F_c exceeds the mixture transport velocity V_{m0}, whereas the local concentration C_{vl} is lower than the feeding concentration C_{v0}. Waterhead H changes slightly under the balance between the energy consumption by mixture–wall interaction and the positive gravity work. With the decrease of the inclined angle and the increase of the curvature near the end of the descending section, the particles are hindered again before going through the trough of the riser, showing an increase of C_{vl} and a decrease of V_{xl}. A reduction of F_c can be found in the first half of the descending section, where the particles have just passed the peak position and become suspended on the upper side of the cross section. Subsequently, a number of particles settle to the lower side of the wall due to gravity and are manifested as bed load in the second half of the descending section, showing a larger F_c. A second extreme $F_c = 88.9$ N ($\approx 1.54 F_b$) occurs at the trough of the riser.

From the perspectives of engineering designs and applications, the overall hydraulic gradient I is an important issue, which is the primary input parameter for the design of a pump. In the present study, the hydraulic gradient of each section is calculated by dividing the difference of the waterheads at both ends by the length of that section, and the results are listed in Table 3. It is observed that the hydraulic gradients in the ascending sections are more than five times those in the descending section, indicating that the energy consumption mainly comes from the ascending section during the mixture transport.

Table 3. Hydraulic gradient during mixture transport.

Section	I (m/m)
overall (P11–P1)	0.115
first ascending (P4–P1)	0.177
descending (P8–P4)	0.034
second ascending (P11–P8)	0.18

In order to capture the detailed dynamic performances of the mixture, the instantaneous flow and particle patterns in the longitudinal and cross sections of typical monitors (P2, P4, P6, P8, P10) are shown in Figures 8–11.

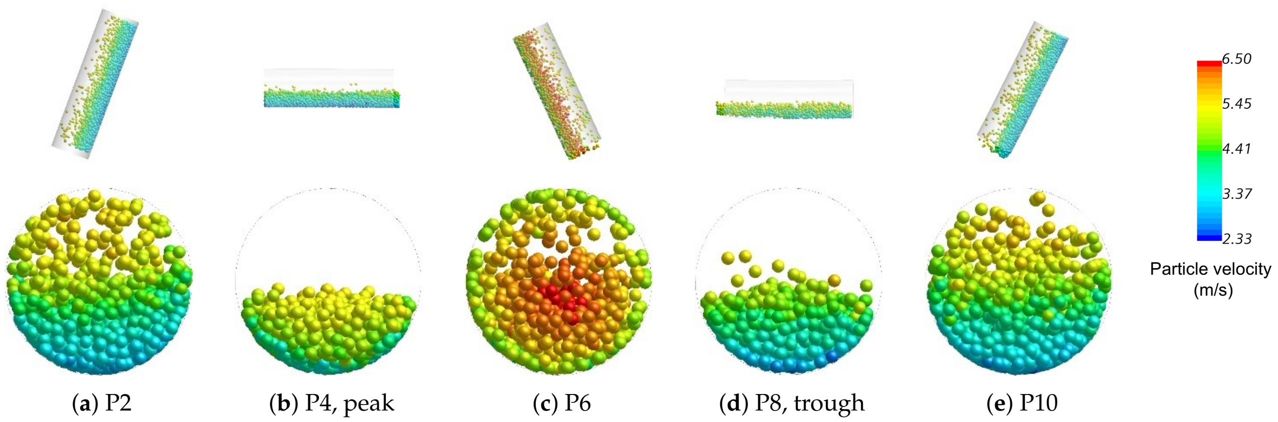

Figure 8. Particle velocity and distribution in longitudinal and cross sections of typical monitors.

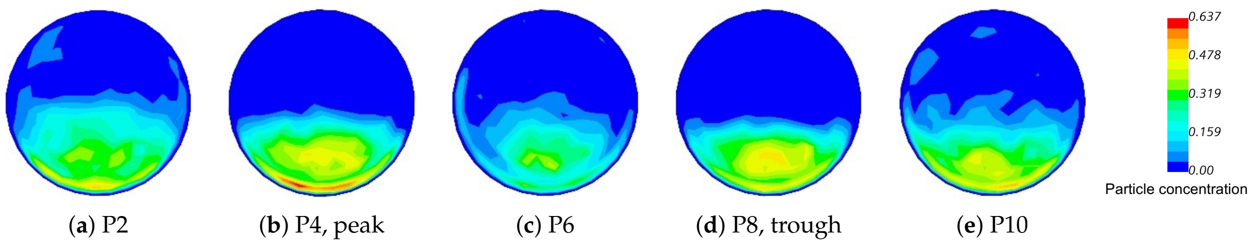

Figure 9. Particle concentration in the cross sections of the typical monitors.

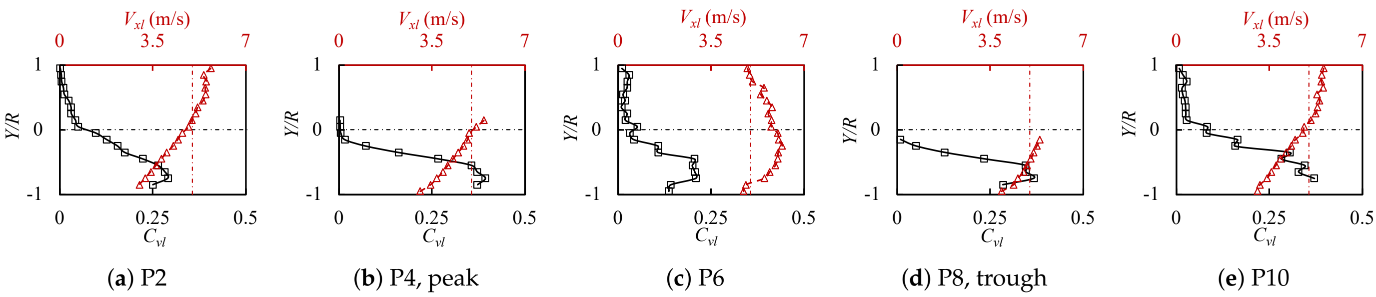

Figure 10. Local concentration and particle velocity in cross sections of the typical monitors. Black hollow square markers represent C_{vl} and red hollow triangle markers represent V_{xl}.

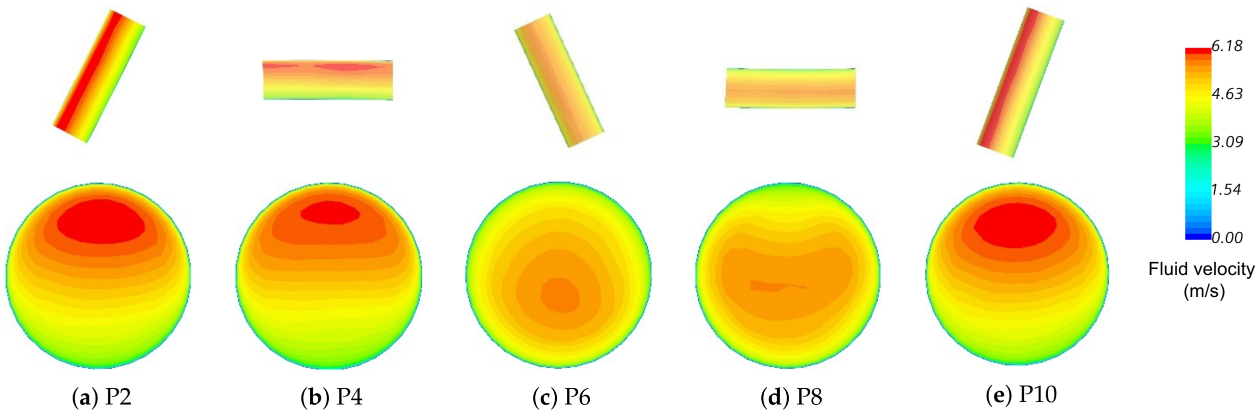

Figure 11. Flow velocity in longitudinal and cross sections of typical monitors.

In ascending sections, particles appear throughout the cross section (Figure 8a,e). However, the mixtures are significantly stratified and movable bed layers are formed [35]. Most of the particles accumulate on the lower side of the riser wall (Figure 9a,e), and are transported as bed load that would experience substantial particle–wall and particle–particle contact forces. This is consistent with the experimental results in the ascending pipelines [10]. In addition, the fluid is significantly decelerated when flows through the porous medium of bed load (Figure 11a,e). This may consequently decrease the fluid resistance acting as the driving force on the particles in the ascending sections. Therefore, the particle velocity of the bed load is small, and almost all the particles on the lower half of the cross section travel at a speed lower than the mixture transport velocity of 5 m/s, as shown by the red labels in Figure 10a,e. A few particles are suspended and transported in the upper side of the cross section. Noting that the suspended particles would fall to the upper layer of the bed load, whereas particles on the top of the bed load would jump up to the turbulent dilute flow. Owing to the large fluid velocity and the finite particle collisions, the suspended particles move faster than the mixture.

At the peak of the riser, the effect of particle settling is more obvious, which is reflected by the few particles observed in the upper side of the cross section, as shown in Figures 8b and 10b. A larger volume fraction of the particles can be observed in the lower side of the cross section when compared to that in the ascending section (Figures 9b and 10b). Generally, the fluid velocity distribution here is similar to that in the ascending section, as shown in Figure 11b. Owing to the large curvature at the peak, the fluid velocity on the upper side is slightly reduced.

In the descending section, particles can be observed all over the cross section and are transported at a fast speed (Figure 8c). The maximum particle velocity occurs in the lower-middle part of the cross section, as indicated in Figures 8c and 10c. A considerable number of particles jump to the upper dilute mixture due to the large particle velocity near the top of the bed load and the violent fluid-particle interaction near the interface.

As a result, the particle volume fraction in the lower part is much smaller than that in the ascending section, as shown in Figures 9c and 10c. The comparisons of C_{vl} in the cross section between the ascending and the descending sections agree well with the results in the experiments [10]. Due to the mass conservation, the reduced particle volume fraction (see Figure 7a) enlarges the area for the fluid to pass through in the cross section, leading to a small average fluid velocity (Figure 11c). It is noticed that the particles in the lower-middle part of the cross section are of close velocity to the fluid, which means that the fluid drag force on the particles may be marginal as a driving force to the particle transport, or even hinders the particles moving downward when the particles travel faster than the surrounding fluid. On the other hand, particle collisions may promote particle transport and enlarge particle velocity to a certain extent.

At the trough of the riser, the mixtures are hindered significantly owing to the large curvature. The suspended particles settle to the top layer of the bed load mostly and aggravate the accumulation in the lower half of the cross section (Figures 9d and 10d). In consequence, the particle volume fraction increases and the particle velocity decreases. However, after a long distance for acceleration in the descending section, the average particle velocity is still larger than that in the ascending section or at the peak, and the particle volume fraction is smaller (Figure 7a,b).

4.2. Effects of Feeding Concentration and Mixture Transport Velocity

The mixture transport velocity V_{m0} and the feeding concentration C_{v0} are significant factors in the dynamics of the inner flow and the hydraulic gradient. In order to examine the effects of these two factors, two series of numerical cases are carried out in the present study. For convenience, local concentration C_{vl}, particle velocity V_{xl}, and particle–wall contact force F_c are non-dimensionalized by C_{v0}, V_{m0}, and F_b, respectively.

Figure 12 shows the calculated results with different feeding concentrations C_{v0}. The overall trends of C_{vl}/C_{v0}, V_{xl}/V_{m0}, and F_c/F_b keep unchanged when C_{v0} is increased from 3% to 12%. This indicates that the maximum local concentration and the minimum particle velocity would always occur in the same positions, which should be considered particularly in the design of the riser. Moreover, C_{vl}/C_{v0} and V_{xl}/V_{m0} would barely change in the range of $C_{v0} \geq 6\%$, illustrating a critical feeding concentration above which the dynamic performances of the mixture may be insensitive to C_{v0}. As more particles are injected into the riser at a larger C_{v0}, the accumulation in the ascending sections becomes more severe and hence the layer of bed load is thicker [35]. This enlarges the probability and frequency of particle–wall interaction. As a result, F_c/F_b is increased, especially near the peak and trough (Figure 12c). On the contrary, more particles would jump up into the dilute mixture from the bed load, and an obvious reduction of F_c/F_b can be observed in the middle part of the descending section.

As shown in Figure 12d, a higher C_{v0} would enlarge the overall hydraulic gradient because of the more energy consumed to do work against gravity and contact during mixture transport. This is consistent with the experimental conclusions for a sea test [36]. Additionally, the increased occupation of the particles would result in a narrow channel for fluid to pass through. The fluid velocity is consequently increased followed by the larger fluid–wall friction and pressure loss. The denser particle flow would result in a larger hydraulic gradient in the ascending section and a smaller one in the descending section. The difference comes from the different effect of gravity on the particles: it prevents particles to move upward in the ascending section, however, becomes a driving force in the descending section. The higher the concentration, the more energy is consumed to lift the particles upward, and the more work the gravity does on the descending mixture.

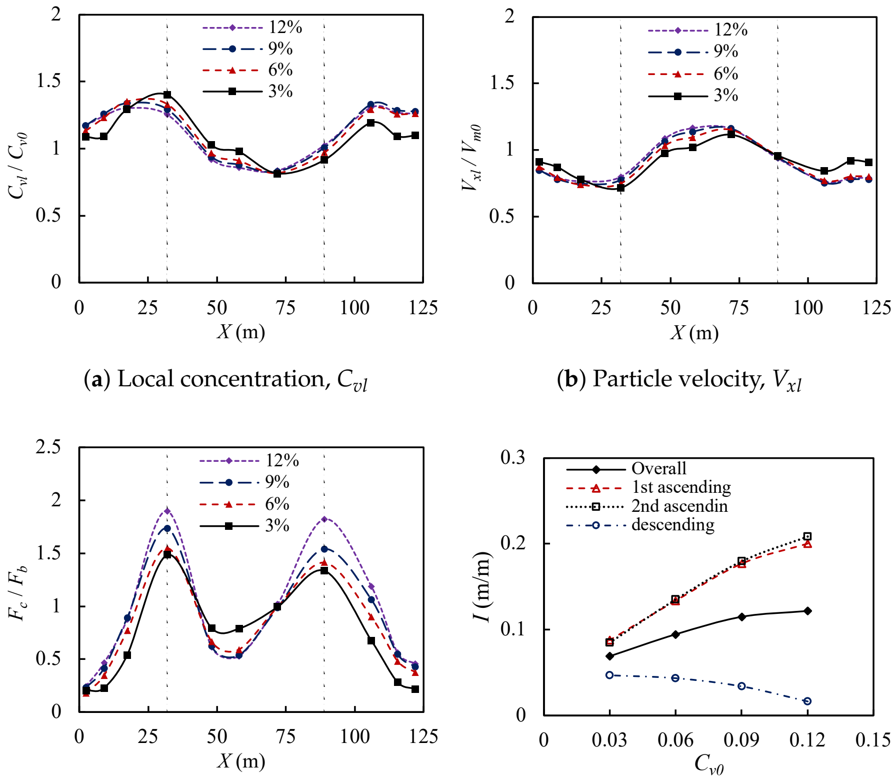

(**a**) Local concentration, C_{vl} (**b**) Particle velocity, V_{xl}

(**c**) Particle–wall contact force, F_c (**d**) Hydraulic gradient, I

Figure 12. Effect of feeding concentration C_{v0} (at $V_{m0} = 5$ m/s).

Figure 13 presents the influence of mixture transport velocity V_{m0} on the dynamic performances of the inner flow. From the perspective of operation safety, a large V_{m0} would be beneficial to the mixture transport according to the small local concentration C_{vl} and the large particle velocity V_{xl} in the ascending sections [37], as shown in Figure 13a,b. On the contrary, the small V_{m0} is quite dangerous and poses a great risk of blockage in engineering applications. For example, at $V_{m0} = 3$ m/s, C_{vl} is even more than 1.5 times C_{v0} in the ascending sections, and V_{xl} is as low as half of V_{m0} ahead of the peak and in the second ascending section. Additionally, a low V_{m0} would aggravate the accumulation of the particles and intensify the particle–wall interaction. Consequently, the particle–wall contact force F_c/F_b would be severe especially at the peak and trough of the riser, as shown in Figure 13c.

In terms of the production efficiency of the system, a high mixture transport velocity is not always better. An excessive flow velocity leads to more pronounced fluid–wall interactions and thus increases the overall hydraulic gradient during the mixture transport (Figure 13d). This puts forward higher requirements on the energy consumption of the system and the performance of transportation facilities such as the pump head. Therefore, a moderate mixture transport velocity (e.g., 4∼5 m/s) in the flexible riser is suggested for the commercial production of deep-sea mining.

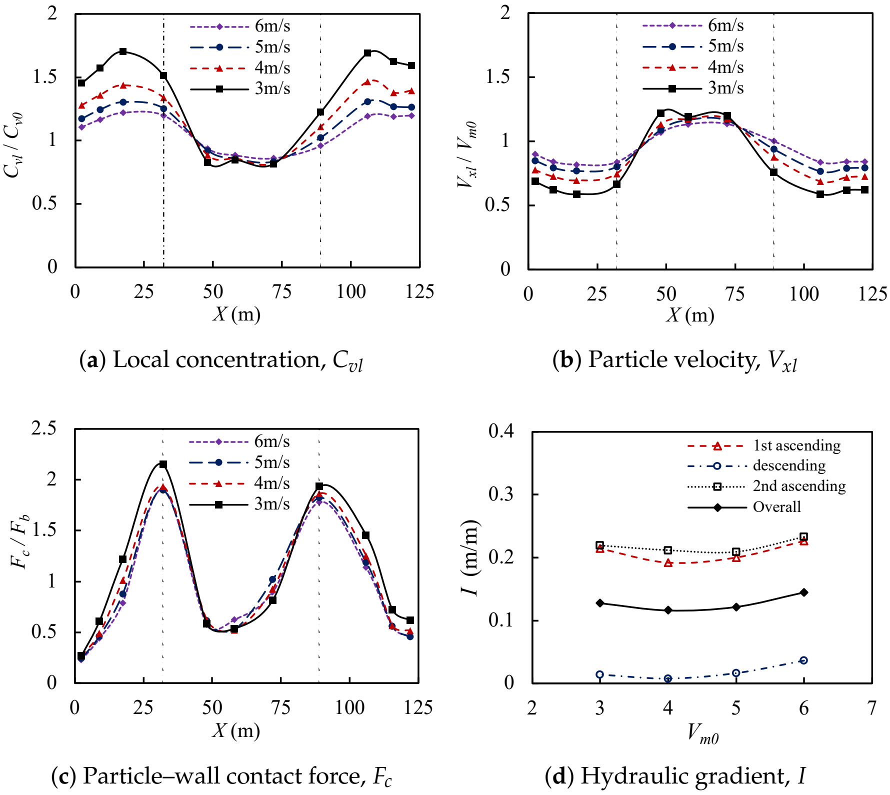

Figure 13. Effect of mixture transport velocity V_{m0} (at $C_{v0} = 12\%$).

4.3. Influence of Riser Configuration

Based on the concerns of operation safety and energy efficiency in engineering applications, another feasible configuration of a flexible riser with two peaks (Figure 14), namely the double-peak riser has been proposed owing to the lower axial tension in the riser, the smaller loads and impacts on the mining vehicle and thus the wider operation areas for the system. Therefore, the mixture in a double-peak riser has been simulated to assess which configuration is more suitable for deep-sea mining from the viewpoint of the inner flow. Except for the spatial configuration, the geometric parameters of the double-peak riser such as the span, the endpoint position, the total length, and the diameter are the same as those of the single-peak one. Both these two configurations depicted in Figure 14a are calculated according to the parameters in an initial design for a deep-sea mining system. In total, 17 monitors are set along the riser to capture the time traces and instantaneous characteristics of the mixtures. The positions of the monitors are listed in Table 4. Intuitively, the double-peak riser seems to be more complicated, because the mixture would travel through two peaks and two troughs which may increase the risk of blockage. However, the calculated results are different from the intuitive grasp.

Figure 15 shows the comparison between the time-averaged characteristics of the mixture in single-peak and double-peak risers at $C_{v0} = 0.09$ and $V_{m0} = 5$ m/s. Generally, the differences between the maximum and the minimum values of C_{vl} and V_{xl} are not significant in both configurations, although the extreme values occur in different positions. Large C_{vl} accompanied by small V_{xl} appears in the ascending sections, whereas the opposite results take place in the descending sections.

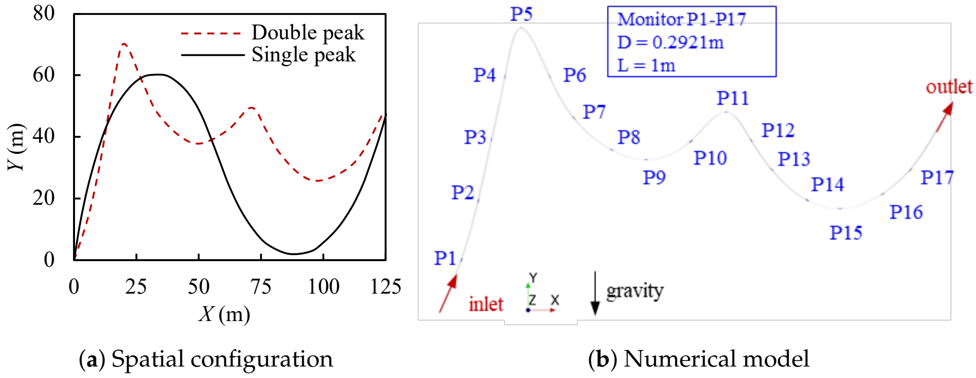

Figure 14. Spatial configuration and numerical model of the double-peak riser.

Table 4. Positions and inclined angles of the monitors in the double-peak riser.

Monitor	Position (x, y) (m)	Inclined Angle (°)	Monitor	Position (x, y) (m)	Inclined Angle (°)
P1	(5.37, 13.14)	74.06	P10	(61.78, 42.30)	37.71
P2	(9.55, 27.77)	77.60	P11	(71.03, 49.46)	0.00
P3	(12.83, 42.71)	78.06	P12	(76.70, 42.57)	−54.77
P4	(16.12, 58.24)	79.68	P13	(81.77, 35.39)	−40.88
P5	(20.00, 70.19)	0.00	P14	(90.43, 27.90)	−14.67
P6	(27.16, 58.24)	−59.60	P15	(98.48, 25.79)	0.00
P7	(33.13, 48.05)	−40.10	P16	(108.93, 29.35)	40.98
P8	(42.38, 40.25)	−16.08	P17	(115.79, 35.31)	56.98
P9	(50.73, 37.85)	0.00			

The first main difference of the mixture transport comes from the spatial shapes of the first ascending sections. In the double-peak riser, the inclination angle of the first section changes slightly, which indicates that this section is similar to a straight pipe with a large inclination angle. The accumulation of particles on the riser wall is then significantly reduced when compared to that in the single-peak riser, and this results in a much smaller particle–wall contact force (Figure 15c). Thereby, the particles can be transported easier by the ambient fluid in the riser, exhibiting the smaller C_{vl}/C_{v0} and the larger V_{xl}/V_{m0} in most parts of this section (Figure 15a,c).

Secondly, the particle–wall contact forces F_c/F_b in different configurations are totally different, or even opposite. In the single-peak riser, the maximum F_c/F_b appears at both the peak and the trough of the riser. However, in the double-peak riser, the minimum F_c/F_b occurs at the peaks, whereas the maximum F_c/F_b arises at the troughs. In the ascending sections of a double-peak riser, the larger inclination angle and the nearly straight riser would result in a significant reduction of particle accumulation on the wall, hence a smaller particle–wall contact. When the particles pass through the peaks to the descending sections, a number of particles would be hindered by the large curvature at the peak and then fall on the wall of the descending section as bed load, resulting in an increase of the particle–wall interaction. Subsequently, the particles in the bed load would be suspended again when passing through the trough due to the obstruction caused by the large curvature. Therefore, the particle–wall contact force is reduced again.

From the perspective of energy consumption, the hydraulic gradient I in the double-peak riser is much smaller than that in the single-peak riser. As the same lifting height of the mixture in both configurations, the hydraulic gradients resulting from the different densities between particles and the fluid are close. The difference in the hydraulic gradient caused by the fluid–wall friction is marginal can be inferred from the close local concentration (based on the laws of mass conservation and the same transport parameters, e.g., C_{v0} and V_{m0} in both configurations). Consequently, one may infer that the considerable reduction of the hydraulic gradient in the double-peak riser is determined by the mitigation of the particle–wall contact.

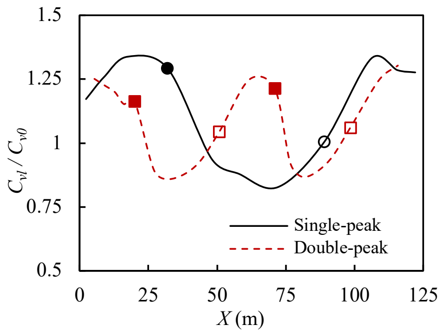

(**a**) Local concentration, C_{vl}

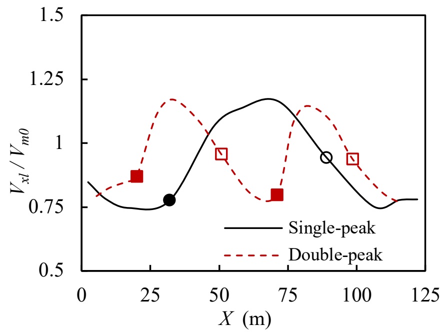

(**b**) Particle velocity, V_{xl}

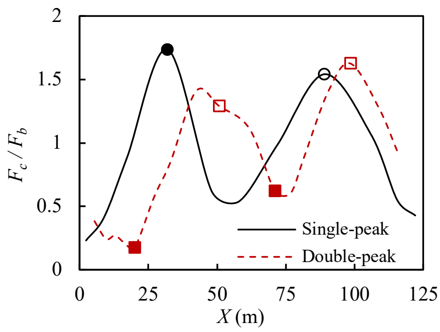

(**c**) Particle–wall contact force, F_c

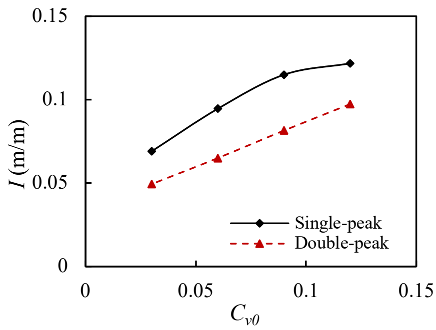

(**d**) Hydraulic gradient, I

Figure 15. Comparison between the mixtures in single-peak and double-peak risers. In (**a**–**c**), the solid markers represent the peak and the hollow markers label the trough.

In addition, a series of cases of the mixture transport in the single-peak and double-peak risers are simulated at different C_{v0} (3%, 6%, 9%, 12%) and V_{m0} (3, 4, 5, 6 m/s). The maximum local concentration $C_{vl,max}/C_{v0}$, the minimum particle velocity $V_{xl,min}/V_{m0}$, the maximum particle–wall contact force $F_{c,max}/F_b$, and the overall hydraulic gradient I in these two different configurations are compared in Figure 16. Compared to the results in the single-peak riser, one can find the lower $C_{vl,max}$, the larger $V_{xl,min}$ and the smaller $F_{c,max}$ in the double-peak riser in most cases. This indicates that there is less risk of particle blockage and riser damage in the double-peak riser, which is more appropriate for the mixture transport from the perspective of safety. On the other hand, the overall hydraulic gradient in the double-peak riser is always lower than that in the single-peak riser in all the cases, illustrating a lower energy consumption and a better performance of the double-peak riser from the viewpoint of energy saving. To sum up, the double-peak riser may be more suitable for the mixture transport in terms of the dynamics of the inner mixture.

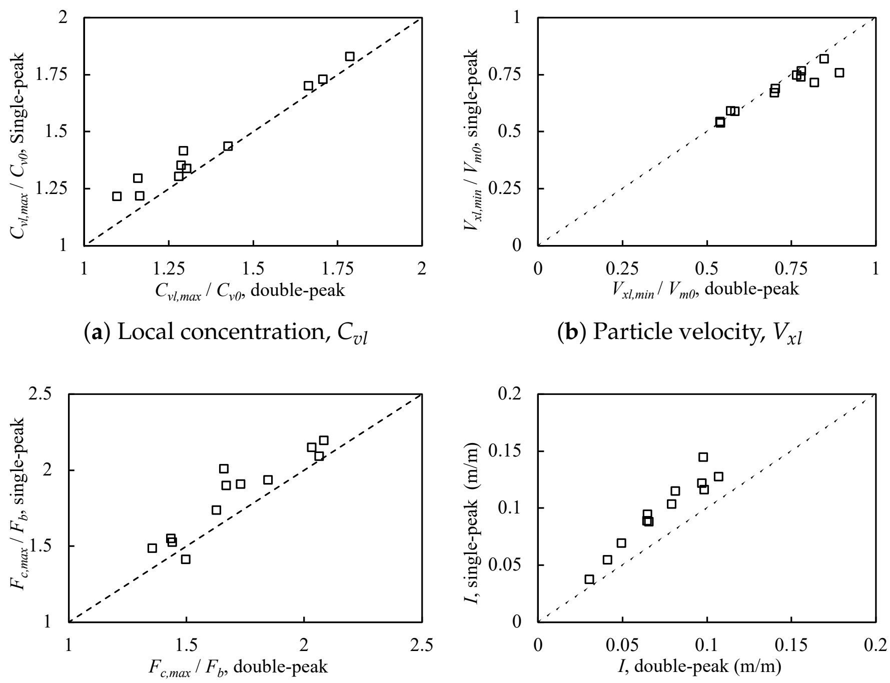

(**a**) Local concentration, C_{vl} (**b**) Particle velocity, V_{xl}

(**c**) Particle–wall contact force, F_c (**d**) Hydraulic gradient, I

Figure 16. Comparison of maximum C_{vl}/C_{v0}, minimum V_{xl}/V_{m0}, maximum F_c/Fb and overall I, single-peak versus double-peak risers.

5. Conclusions

Based on the background of deep-sea mining applications in engineering, a numerical investigation of the dynamics of mixture transport in a flexible riser was conducted using CFD-DEM. The time-averaged and instantaneous in situ characteristics, e.g., local concentration, particle velocity, and particle–wall contact, have an in-depth "understanding" of the inner mixture. Sensitivity analyses on the key parameters were performed to evaluate the effects on the mixture transport. Finally, the mixtures in the single-peak and double-peak risers were compared to find a better spatial configuration for deep-sea mining. The main conclusions are summarized as follows.

(1) In a single-peak flexible riser, there is a greater risk of particle blockage in the ascending sections, particularly ahead of the peak, according to the large local concentration ($\approx$1.34 C_{v0}) and the small particle velocity ($\approx$0.75 V_{m0}) resulting from particle accumulation on the riser wall.

(2) At the peak and the trough of the single-peak riser, the maximum particle–wall contact forces ($\approx$1.74 F_b and 1.54 F_b, respectively) are observed owing to the large curvature. This should be "noticed" to avoid damage to the riser.

(3) The hydraulic gradient mainly comes from the ascending sections, where the particle–wall contact is severe on the lower side and the fluid–wall interaction is intense on the upper side of the riser.

(4) A small feeding concentration (e.g., $C_{v0} \leq 6\%$) would reduce both particle–wall contact and overall hydraulic gradient, whereas a moderate transport velocity (e.g., 4$\sim$5 m/s) is appropriate for the mixture transport by considering both operational safety and energy consumption.

(5) Compared to the single-peak riser, a double-peak configuration would be better for deep-sea mining owing to the lower local concentration, the larger particle velocity, and the smaller overall hydraulic gradient.

Author Contributions: Conceptualization, L.L. and X.G.; methodology, L.L. and K.G.; software, L.L. and K.G.; validation, L.L. and J.Y.; formal analysis, L.L. and K.G.; investigation, L.L., K.G. and X.G.; resources, L.L. and J.Y.; data curation, L.L., K.G. and J.Y.; writing—original draft preparation, L.L. and X.G.; writing—review and editing, L.L. and X.G.; visualization, L.L. and J.Y.; supervision, J.Y.; project administration, L.L.; funding acquisition, L.L. All authors have read and agreed to the published version of the manuscript.

Funding: This research was supported by the National Natural Science Foundation of China (grant no: 51909164) and the Hainan Provincial Joint Project of Sanya Yazhou Bay Science and Technology City (grant no: 520LH052).

Institutional Review Board Statement: Not applicable.

Informed Consent Statement: Not applicable.

Data Availability Statement: The data presented in this study are available from the corresponding author upon request.

Acknowledgments: The authors would like to thank the reviewers and editors for their constructive suggestions to improve the quality of the paper.

Conflicts of Interest: The authors declare no conflict of interest.

References

1. Murray, J.; Renard, A.F. *Report on Deep-Sea Deposits Based on the Specimens Collected during the Voyage of H.M.S. Challenger in the Years 1872 to 1876*; John Menzies and Co.: Edinburgh, UK, 1891; pp. 184–186.
2. Toro, N.; Robles, P.; Jeldres, R.I. Seabed mineral resources, an alternative for the future of renewable energy: A critical review. *Ore Geol. Rev.* **2020**, *126*, 103699. [CrossRef]
3. Hannington, M.; Petersen, S.; Kratschell, A. Subsea mining moves closer to shore. *Nat. Geosci.* **2017**, *10*, 158–159. [CrossRef]
4. Leng, D.; Shao, S.; Xie, Y.; Wang, H.; Liu, G. A brief review of recent progress on deep sea mining vehicle. *Ocean Eng.* **2021**, *228*, 108565. [CrossRef]
5. Hein, J.R.; Mizell, K.; Koschinsky, A.; Conrad, T.A. Deep-ocean mineral deposits as a source of critical metals for high- and green-technology applications: Comparison with land-based resources. *Ore Geol. Rev.* **2013**, *51*, 1–14. [CrossRef]
6. Mero, J.L. *The Mineral Resources of the Sea*; Elsevier Oceanography Series; Elsevier: Amsterdam, The Netherlands, 1965; Volume 1.
7. Willums, J.O.; Bradley, A.O. M.I.T.'s Deep sea mining project. In Proceedings of the Offshore Technology Conference, Houston, TX, USA, 6–8 May 1974.
8. Engelmann, H.E. Vertical hydraulic lifting of large-size particles—A contribution to marine mining. In Proceedings of the Offshore Technology Conference, Houston, TX, USA, 8–11 May 1978.
9. Oh, J.W.; Jung, J.Y.; Hong, S. On-board measurement methodology for the liquid-solid slurry production of deep-seabed mining. *Ocean Eng.* **2018**, *149*, 170–182. [CrossRef]
10. Vlasak, P.; Chara, Z.; Konfrst, J. Flow behaviour and local concentration of coarse particles-water mixture in inclined pipes. *J. Hydrol. Hydromech.* **2017**, *65*, 183–191. [CrossRef]
11. Xia, J.; Ni, J.R.; Mendoza, C. Hydraulic lifting of manganese nodules through a riser. *J. Offshore Mech. Arct. Eng. Trans. ASME* **2004**, *126*, 72–77. [CrossRef]
12. Wu, Q.; Yang, J.; Lu, H.; Lu, W.; Liu, L. Effects of heave motion on the dynamic performance of vertical transport system for deep sea mining. *Appl. Ocean Res.* **2020**, *101*, 102188. [CrossRef]
13. Parenteau, T.; Lemaire, A. Flow assurance for deep ocean mining—Pressure requirement through S-shape riser and jumper. In Proceedings of the Offshore Technology Conference, Houston, TX, USA, 2–5 May 2011.
14. Yoon, C.H.; Kwon, K.S.; Kwon, S.K.; Lee, D.K.; Park, Y.C.; Kwon, O.K.; Sung, W.M. An experimental study on the flow characteristics of solid-liquid two-phase mixture in a flexible hose. In Proceedings of the 4th ISOPE Ocean Mining Symposium, Szczecin, Poland, 23–27 September 2001.
15. Yao, N.; Cao, B.; Xia, J. Pressure loss of flexible hose in deep-sea mining system. In Proceedings of the 18th International Conference on Transport and Sedimentation of Solid Particles, Prague, Czech Republic, 11–15 September 2017.
16. Wang, Z.; Rao, Q.; Liu, S. Fluid-solid interaction of resistance loss of flexible hose in deep ocean mining. *J. Cent. South Univ.* **2012**, *19*, 3188–3193. [CrossRef]
17. Yu, A.; Cheng, Y.; Eason, R. Slurry flow simulation for deepwater mining application. In Proceedings of the 29th International Conference on Offshore Mechanics and Arctic Engineering, Shanghai, China, 6–11 June 2010.
18. Peng, Y.; Xia, J.; Cao, B.; Ren, H.; Wu, Y. Spatial configurations and particle transportation parameters of flexible hose in deep-sea mining system. In Proceedings of the 25th International Ocean and Polar Engineering Conference, Kona, WA, USA, 21–27 June 2015.

19. Yoon, C.H.; Kang, J.S.; Park, Y.C.; Kim, Y.J.; Park, J.M.; Kwon, S.K. Solid-liquid Flow Experiment with Real and Artificial Manganese Nodules in Flexible Hoses. In Proceedings of the 18th International Offshore and Polar Engineering Conference, Vancouver, BC, Canada, 6–11 July 2008.
20. Ramesh, N.R.; Thirumurugan, K.; Rajesh, S.; Deepak, C.R.; Atmanand, M.A. Experimental and computational investigation of turbulent pulsatile flow through a flexible hose. In Proceedings of the 10th ISOPE Ocean Mining and Gas Hydrates Symposium, Szczecin, Poland, 22–26 September 2013.
21. Parenteau, T. Flow assurance for deepwater mining. In Proceedings of the 29th International Conference on Offshore Mechanics and Arctic Engineering, Shanghai, China, 6–11 June 2010.
22. Dai, Y.; Zhang, Y.; Li, X. Numerical and experimental investigations on pipeline internal solid-liquid mixed fluid for deep ocean mining. *Ocean Eng.* **2021**, *220*, 108411. [CrossRef]
23. Chen, Q.; Xiong, T.; Zhang, X.; Jiang, P. Study of the hydraulic transport of non-spherical particles in a pipeline based on the CFD-DEM. *Eng. Appl. Comp. Fluid Mech.* **2020**, *14*, 53–69. [CrossRef]
24. Zhou, M.; Wang, S.; Kuang, S.; Luo, K.; Fan, J.; Yu, A. CFD-DEM modelling of hydraulic conveying of solid particles in a vertical pipe. *Powder Technol.* **2019**, *354*, 893–905. [CrossRef]
25. Ravelet, F.; Bakir, F.; Khelladi, S.; Rey, R. Experimental study of hydraulic transport of large particles in horizontal pipes. *Exp. Therm. Fluid Sci.* **2013**, *45*, 187–197. [CrossRef]
26. Hu, Q.; Zou, L.; Lv, T.; Guan, Y.; Sun, T. Experimental and numerical investigation on the transport characteristics of particle-fluid mixture in Y-shaped elbow. *J. Mar. Sci. Eng.* **2020**, *8*, 675. [CrossRef]
27. Hu, Q.; Chen, J.; Deng, L.; Kang, Y.; Liu, S. CFD-DEM simulation of backflow blockage of deep-sea multistage pump. *J. Mar. Sci. Eng.* **2021**, *9*, 987. [CrossRef]
28. Yang, D.; Xia, Y.; Wu, D.; Chen, P.; Zeng, G.; Zhao, X. Numerical investigation of pipeline transport characteristics of slurry shield under gravel stratum. *Tunn. Undergr. Space Technol.* **2018**, *71*, 223–230. [CrossRef]
29. Di Felice, R. The voidage function for fluid-particle interaction systems. *Int. J. Multiph. Flow* **1994**, *20*, 153–159. [CrossRef]
30. Sommerfeld, M. *Theoretical and Experimental Modelling of Particulate Flows*; Technical Report Lecture Series 2000-06; von Karman Institute for Fluid Dynamics: Sint-Genesius-Rode, Belgium, 2000; pp. 20–23.
31. Auton, T.R.; Hunt, J.C.R.; Prud'Homme, M. The force exerted on a body in inviscid unsteady non-uniform rotational flow. *J. Fluid Mech.* **1988**, *197*, 241–257. [CrossRef]
32. Johnson, K.L. *Contact Mechanics*; Cambridge University Press: Cambridge, UK, 1985.
33. Di Renzo, A.; Di Maio, F.P. Comparison of contact-force models for the simulation of collisions in DEM-based granular flow codes. *Chem. Eng. Sci.* **2004**, *59*, 525–541. [CrossRef]
34. Tsuji, Y.; Tanaka, T.; Ishida, T. Lagrangian numerical simulation of plug flow of cohesionless particles in a horizontal pipe. *Powder Technol.* **1992**, *71*, 239–250. [CrossRef]
35. Vlasak, P.; Chara, Z.; Krupicka, J.; Konfrst, J. Experimental investigation of coarse particles-water mixture flow in horizontal and inclined pipes. *J. Hydrol. Hydromech.* **2014**, *62*, 241–247. [CrossRef]
36. Yoon, C.H.; Lee, D.K.; Park, Y.C.; Kim, Y.J.; Kwon, S.k. Flow analysis of lifting pump and flexible hose for sea-test. In Proceedings of the 16th International Offshore and Polar Engineering Conference, San Francisco, CA, USA, 28 May–2 June 2006.
37. Vlasak, P.; Chara, Z.; Konfrst, J.; Krupicka, J. Effect of concentration and velocity on conveying of coarse grained mixtures in pipe. In Proceedings of the 24th International Ocean and Polar Engineering Conference, Busan, Republic of Korea, 15–20 June 2014.